**Main manuscript for**

# Quantitative measurement of microbial growth rate with Raman microspectroscopy

Tristan A. Caro *[1], Srishti Kashyap [1], George Brown [2], Claudia Chen [2], Sebastian H. Kopf [1], Alexis S. Templeton [1]

1. Department of Geological Sciences, University of Colorado Boulder
2. Department of Statistics, University of Colorado Boulder

*** Corresponding Author**
Tristan Caro
2200 Colorado Ave
Benson Earth Sciences Building
Rm. 285. UCB 399
Boulder, CO 80309
tristan.caro@colorado.edu

**Competing interest statement:** The authors declare no conflicts of interest.

**This file includes:**

Main Text
Figures 1 - 4
Tables 1 - 2
References

## Abstract

Rates of microbial activity and growth are fundamental to understanding environmental geochemistry and ecology. However, measuring the heterogeneity of microbial activity at the single-cell level, especially within complex populations and environmental matrices, remains a forefront challenge. Stable Isotope Probing (SIP) is a standard method for assessing microbial activity and involves measuring the incorporation of an isotopically labeled compound into microbial biomass. Here, we assess the utility of Raman microspectroscopy as a SIP technique, specifically focusing on the measurement of deuterium ($^{2}H$), a tracer of microbial biomass production. We generate calibrations of microbial biomass $^{2}H$ values and find that Raman microspectroscopy reliably quantifies $^{2}H$ incorporation ranging between 0 and 40 at. %. Applying the results of this calibration to a SIP model, we explicitly parameterize the factors controlling microbial growth quantification, demonstrating how Raman-SIP can measure the growth of microorganisms with doubling times ranging from hours to years. Furthermore, we correlatively compare our Raman-derived measurements with those of nanoscale secondary ion mass spectrometry (nanoSIMS) to compare the relative strengths of nanoSIMS- and Raman-based SIP approaches. We find that Raman microspectroscopy is a robust, accessible methodology that can readily differentiate and quantify the growth of individual microbial cells in complex samples.

## Introduction

Microbial growth rate is a critical parameter for assessing biogeochemical cycling, environmental habitability, and microbial fitness. Not only does the rate of microbial growth represent a geochemical transformation, but it is also a parameter that microorganisms modulate in response to changing conditions: microorganisms may more readily replicate when conditions are favorable to them and adopt alternative physiologic states under adverse conditions.

Methods for measuring microbial growth in environmental systems often rely upon the addition of an isotopically labeled substrate to a natural sample and measuring its incorporation into microbial biomass, a method generally termed stable isotope probing (SIP) (1–3). SIP has been applied with the stable isotopes of various elements including H, C, N, O, S, etc., through measurement of single-cells (4–8), membrane lipids (3,9,10), and nucleic acids (2,11–13). One approach to probe cellular biosynthesis is to amend an environmental sample with deuterated water ($^2H_2O$) (3–6,8,10,14–18). Water is incorporated into microbial biomass during the synthesis of lipids, nucleic acids, and proteins, and so probing a sample with deuterated water allows the quantification of microbial biomass growth. $^2H_2O$ has been termed a "passive" tracer for microbial anabolism, as it is nutritionally neutral and taxonomically agnostic.

In microbial communities, spatial relationships dictate ecological and evolutionary dynamics, as well as community structure and function (26–30). However, microbial growth is known to be extremely heterogenous in environments such as soil matrices (30), marine particles, (31–33), the rock-hosted subsurface (34,35) and others. Spatially-resolved measurements of microbial growth can identify the habitability and biological activity of environmental samples at the microscale. Furthermore, single-cell measurements of microbial growth are especially useful

for microbial ecologists as they provide information on anabolic heterogeneity across and within populations. However, describing the spatial distributions of microorganisms in the environment, in addition to their degrees of activity, remains one of the primary challenges in microbial ecology.

Nanoscale secondary ion mass spectrometry (nanoSIMS) is a standard method for conducting spatially-resolved SIP measurements of individual cells (4,6,7,10,15,18,36–39). NanoSIMS relies on the measurement of secondary ions released via ablation by a primary ion beam and measures isotopes of multiple elements at high spatial resolution. However, isotope ratios measured via nanoSIMS may become depressed due to the inclusion of stains, nucleic acid probes, and sample washing (40–42). Additionally, nanoSIMS remains a costly and time intensive method that is inaccessible to many researchers. We therefore set out to assess alternative methodologies that may circumvent these difficulties.

In 2015, foundational work by Berry and colleagues established Raman microspectroscopy as a viable tool for detecting deuterium enrichment of microbial biomass at the single-cell level (8). Raman-based measurements of deuterium in microbial biomass rely on the principle that there exists a strong band centered at 2800 $cm^{-1}$, corresponding to C-H bonding environments associated with lipids, proteins, and nucleic acids of cells. When deuterium is incorporated into microbial biomass, this band, now representing C-$^{2}$H ("C-D") bonds, becomes red-shifted and centers at 2200 $cm^{-1}$ **(Fig. 1B)**. In previous work, the "CD% metric", defined as the fractional abundance of CD and CH peak areas, (CD% = CD / (CD + CH) × 100%) was found to correlate with the deuterium fractional abundance ($^{2}F$) of the growth medium provided to the organisms (8). Berry et al. illustrated applications of Raman-SIP in combination with fluorescence in situ hybridization

(FISH) and cell-sorting methodologies to capture the identity of active microbial community members.

For our study, we built upon this prior work in four key aspects. First we generated a robust hydrogen isotopic calibration for Raman spectroscopy that specifically targets two environmentally-relevant taxa **(Fig. 2)**. Second, we combined the results of our isotopic calibration with a numerical model of microbial growth to determine the feasibility and sensitivity of Raman-SIP for quantitative inference of microbial biomass growth rate **(Fig. 3)**. The ability to translate Raman-derived measurements of deuterium enrichment into biomass synthesis/growth estimates would pave the way for future investigations to not only identify microbial activity *in situ*, but also to quantify biosynthetic growth rate. Third, the cells used to generate our Raman-based isotopic calibration were correlatively measured by nanoSIMS to determine the extent to which nanoSIMS and Raman-based measurements agree. Finally, we provide a computational framework for Raman-SIP that allows users to optimize SIP incubations for their specific study system.

## Results and Discussion

### *Single-cell isotopic measurements*

To assess the sensitivity and precision of Raman microspectroscopy as a reporter of cellular $^2H$ incorporation, we generated a large isotopic dataset of bacterial and archaeal cells grown to equilibrium with deuterated ($^2H_2O$) media of varying hydrogen isotope compositions (0 – 50 at. % $^2H$). We focused our study on two anaerobic organisms isolated from the subsurface biosphere: a sulfate reducing bacterium (SRB) *Thermodesulfovibrio hydrogeniphilus* (43), and a methanogenic archaeon *Methanobacterium NSHQ04* (44). We acquired individual measurements of cellular

deuterium enrichment (n = 351) with Raman spectroscopy and nanoSIMS **(Fig. 1)**. We refer to hydrogen isotope content using both Raman and nanoSIMS as the fractional abundance of deuterium, $^2F$, reported in atom percent (at. %) (see *Materials and Methods*), where $^2F = {}^2H / (H + {}^2H) \times 100\ \%$. To generate hydrogen isotope calibrations, we fit simple linear models relating the hydrogen isotopic composition of microbial biomass ($^2F_{biomass}$) to the organism's growth water ($^2F_{gw}$). (**Fig. 2**).

With Raman microspectroscopy, biomass $^2H$ enrichment ($^2F_{biomass}$) increased linearly and exhibited strong positive correlation ($R^2$ = 0.94, 0.95, for *T. hydrogeniphilus and M. NSHQ04,* respectively) with the deuterium content of the growth water ($^2F_{gw}$) (**Fig. 2, Table 1B**). Raman measurements of biomass deuterium content exhibited an average standard deviation of $\sigma_{2F}$ = 2.89 at. %. The variability of Raman-derived $^2F_{biomass}$ increased with the isotopic composition of the growth water: a maximum standard deviation was observed at the $^2F_{gw}$ = 50% $^2H_2O$ condition where $\sigma_{2F}$ = 3.77 at. %. Corresponding measurements by nanoSIMS of the same cells followed a similar trend: $^2F_{Biomass}$ increased linearly with the growth water applied ($R^2$ = 0.84, 0.96 for *T. hydrogeniphilus* and *M. NSHQ04*, respectively) and the average standard deviation of nanoSIMS $^2F$ was $\sigma_{2F}$ = 1.86 at. %. Similar to Raman, the standard deviation of nanoSIMS measurements increased along with the isotopic composition of growth water, reaching a maximum at the 50% label where $\sigma_{2F}$ = 3.20 at. % (**Table 1A**). With both analytical techniques and across both organisms, we observed depressed biomass enrichments at $^2F_{gw}$ = 50 at. %, likely resulting from deuterium toxicity effects (see section *Applying Raman microspectroscopy to SIP growth rate measurements*). For analytical uncertainty, we report the average standard deviation observed in Raman and nanoSIMS measurements across growth water conditions: 2.89 and 1.86 at. %,

respectively. We emphasize that these are conservative over-estimates of analytical error due to heterogeneity in the hydrogen isotopic enrichment of individual cells. Our data support previous observations by Berry et al. that point to high reproducibility of single-cell measurements (8).

### *Applying Raman microspectroscopy to SIP growth rate measurements*

Having generated a Raman-based hydrogen isotopic calibration of microbial biomass, we sought to test the applicability of this analytical method to measurements of cell-specific growth rate. Microbial growth rate can be inferred from SIP incubations because the degree of an organism's biomass isotopic enrichment over time depends on the isotopic composition of a given substrate and its rate of biomass synthesis (14). Therefore, if measurements of $^{2}H$ incorporation are reliable, then these values should translate to cell-specific growth rates. To this end, we sought to parameterize sources of uncertainty and propagation to downstream calculations to define acceptable experimental conditions and analytical uncertainties for quantitative measurement of microbial growth rate.

The growth rate of an organism in the presence of a stable isotope tracer is calculated with **Eq. 1** (14). In brief, microbial growth rate is a logarithmic relationship between an organism's isotopic composition at the start of an incubation ($F_0$) and its isotopic composition at the time ($t$) of sampling ($F_T$). Cellular isotopic enrichment is compared to the enrichment of the isotopic label ($F_L$) offset by a water hydrogen assimilation efficiency constant ($a_w$) – a value representing the fraction of biomass hydrogen that a cell acquires from its growth water, as opposed to other metabolic sources and associated fractionation effects.

$$\mu = -\frac{1}{t} \cdot ln\left(\frac{F_T - a_w \cdot F_L}{F_0 - a_w \cdot F_L}\right) \quad \text{(Eq. 1)}$$

We modeled growth rates ($\mu$) (**Eq. 1**) across a wide range of SIP experimental conditions (varying $F_L$, $t$, and $a_w$,) and applied standard propagation of uncertainty to determine the associated errors ($\sigma_\mu$) (**Eq. 2**) that result from compounding uncertainty of Raman-SIP experimental aspects (3,14):

$$\sigma_\mu = \frac{\sqrt{(a_w F_L - F_T)^2 \sigma_{F_0}^2 + (a_w F_L - F_0)^2 \sigma_{F_T}^2 + a_w{}^2 \cdot (F_0 - F_T)^2 \sigma_{F_L}^2 + F_L^2 \cdot (F_0 - F_T)^2 \sigma_{a_w}^2}}{t \cdot (a_w F_L - F_0) \cdot (a_w F_L - F_T)} \quad \text{(Eq. 2)}$$

Where sigma ($\sigma$) terms represent uncertainties of each subscripted parameter (e.g., $\sigma_{FT}$ represents uncertainty in biomass isotopic composition at time of sampling $T$). We convert growth rate to biomass generation time using the relationship:

$$T_G = \frac{\ln(2)}{\mu} \quad \text{(Eq. 3)}$$

where $\mu$ is growth rate in units of $t^{-1}$ and $T_G$ is generation time in units of $t$.

To a first order, the range of growth rates ($\mu$) that can be measured with SIP depends on the isotopic composition of the label and the incubation duration. Uncertainty in growth rate ($\sigma_\mu$) depends on analytical uncertainty in label strength ($\sigma_{FL}$), analytical uncertainty of biomass isotopic enrichment ($\sigma_{FT}$), and microbial water hydrogen assimilation efficiency ($\sigma_{aw}$). Our model constrains the region of quantification for both isotopic enrichment (**Fig. 3C**) and corresponding

growth rate (**Fig. 3D-E**) in Raman SIP experiments. We propagate the uncertainty estimates of $^{2}F_{biomass}$ estimated from our hydrogen isotope calibration as $\sigma_{FT}$ to estimate associated uncertainty in growth rate ($\sigma_{\mu}$) that results from a given SIP experiment. We report uncertainty in growth rate relative to the growth rate itself as $Relative\ Error = (\sigma_{\mu} / \mu) \times 100\%$. We set our limit for relative error to be 50% such that errors below this cutoff result in growth rate differences that are distinguishable with > 2σ confidence.

In **Fig. 3** we display example outputs from our model using incubation times of $t = 5$ and $t = 30\ days$ across a range of $^{2}H_2O$ label strengths. For example, the range of quantification for an experiment applying a 35% label is 6.9 - 32.6 at. % deuterium enrichment. Ranges of quantification and error optima for additional isotopic label strengths are reported in **Table 2.** For a 5-day incubation, this range of $^{2}F$ quantification corresponds to growth rates between 0.53 – 0.04 $d^{-1}$, or generation times of 1.3 and 17 days. For a 30-day incubation, this range of $^{2}F$ quantification corresponds to growth rates between 0.09 - 0.007 $d^{-1}$ or generation times between 7.7 and 101.9 days (**Fig. 3E**).

Asymptotic rises in uncertainty at high and low biomass isotopic enrichment, respectively, correspond to (i) uncertainty in growth rate as cell isotopic enrichment approaches that of the label solution and (ii) uncertainty resulting from biomass isotopic signal not significantly exceeding that of the noise inherent to the analytical method. The first condition (i) represents cells that grow faster than can be discriminated using the set incubation time and label strength, while (ii) represents cells that grow too slow to be distinguished from noise. It should be noted that our ranges of quantification should be viewed conservative estimates, as the source of uncertainty we apply corresponds to heterogeneity of $^{2}H$-incorporation across homogenous cell populations, as

opposed to the error across individual Raman acquisitions. This latter source of error is far smaller both in our dataset and in previously reported datasets (8).

Incubation time (*t*) shifts the dynamic range of SIP (**Supplementary Fig. S8**): shorter incubations can resolve faster-growing organisms from each other but may not capture slower-growing organisms due to insufficient label incorporation. Conversely, longer incubations can capture slower-growing organisms, but faster-growing organisms may become saturated with the label and will no longer be resolvable from each other (**Fig. 3**). Growth rates of fast-growing organisms, those that are readily saturated with deuterium, could lead to underestimates of aggregate microbial turnover.

Increasing the strength of the label ($F_L$) expands the dynamic range of the SIP method i.e., both slower and faster growth rates can be captured as there is more isotopic "space" that can be measured (**Table 2, Fig. 3**). However, increasing $F_L$ must be weighed against the risk that higher deuterium concentrations can impose toxicity or unintended physiological effects. Deuterated water at high levels of isotopic labeling have been shown to have no effect, inhibition and even stimulation among different microorganisms (8,10,45). In our experiments, we observed depressed isotopic enrichment in growth water containing *50 at. %* $^2H_2O$. These effects were noted for both organisms and both the Raman and nanoSIMS data (grey point intervals in **Fig. 2**). We conjecture that this result stems from isotopic toxicity affecting microbial growth or metabolic switching at high isotopic enrichment, but this mechanism cannot be explained by our study. Therefore, we caution against applying $^2H_2O$ label strengths at or above 50 at. % due to varying physiological effects that may arise at this threshold, especially when applying this approach to natural microbial communities of unknown and mixed composition. Uncertainties in isotopic label

strength ($\sigma_{FL}$), especially at high isotopic enrichment, due to pipetting or gravimetric dilution contribute relatively minor components to total uncertainty.

The water hydrogen assimilation efficiency constant ($a_w$) is essential for estimation of microbial growth rate, as it sets the upper limit of biomass deuterium enrichment. This limit is represented by the $a_w \cdot F_L$ terms in **Eq. 1 (Fig 3A)**. Therefore, similar to increasing the strength of the label, an organism with a greater $a_w$ has more isotopic "space" in which to become enriched. In our study, we use Raman-derived $^2F$ measurements to empirically determine the $a_w$ of *T. hydrogeniphilus* and *M. NSHQ04* to be $a_w = 0.76 \pm 0.02$ and $a_w = 0.88 \pm 0.02$, respectively (**Table 1C**, **Fig. 2**). The higher $a_w$ observed with the methanogen *M. NSHQ04* is in line with primarily autotrophic growth (44) with an offset from $a_w = 1$ due to hydrogen isotopic fractionation. The slightly lower $a_w$ for the sulfate reducing *T. hydrogeniphilus* is indicative of a hydrogen contribution from its acetotrophic metabolism or from greater fractionation effects. We note that these values represent $a_w$ of whole-cell biomass, which may be distinct from those calculated via compound-specific analysis (3,21,25). It was previously noted that uncertainty in $a_w$ is a significant driver of uncertainty in hydrogen SIP-derived growth rate estimates (3). For mixed communities, this uncertainty must be propagated through growth rate calculations. For organisms with known metabolisms, this term can be estimated as common metabolic modes often constrain $a_w$ factor to a degree (3,21,25).

***Raman and nanoSIMS measure different pools of cellular hydrogen.***

Currently, nanoscale secondary ion mass spectrometry (nanoSIMS) serves as a standard method for reporting single-cell isotope ratios. A NanoSIMS instrument applies a primary ion beam to

ionize and ablate a sample, inducing the release of secondary ions whose isotopic composition is measured by magnetic sector isotope ratio mass spectrometry. NanoSIMS has many benefits as an analytical technique: it can measure multiple isotopes simultaneously and allows spatial/elemental imaging at the nanoscale. However, nanoSIMS destroys the sample and is time and cost-intensive. Furthermore, depression of isotopic enrichment measured by nanoSIMS due to sample preparation has been widely reported for multiple stable isotope tracers ($^{13}C$, $^{18}O$, $^{15}N$, $^{2}H$, and $^{34}S$) under various fixation and staining conditions (8,10,15,36,40–42,46). Given these limitations, it would be useful to have additional methods that can complement the strengths of nanoSIMS while negating some of its drawbacks.

Deuterium enrichments measured by Raman were greater than those measured by nanoSIMS, when compared to the culture growth water (**Fig. 2**). When we correlated cell-specific $^{2}F_{biomass}$ measurements we observed that, cell-to-cell, nanoSIMS-derived hydrogen isotope values were severely depressed compared to corresponding Raman-derived values (**Supplemental Fig. 2**). From this correlative dataset, we calculated an average hydrogen isotope dilution factor of 58.7 ± 6.0 % across all growth water labeling conditions (*Supplementary Text*).

Such a significant dilution of hydrogen isotopes speaks to a fundamental difference in the nature of nanoSIMS- and Raman-based measurements. Owing to how the primary ion beam ionizes and ablates a cell, nanoSIMS is mostly agnostic to the sources of $^{2}H/^{1}H$ it measures, setting aside potential differences in hydrogen ionization efficiency across different classes of molecules. Therefore, $^{1}H^{-}$ and $^{2}H^{-}$ ions reaching the instrument detectors can derive from a variety of cellular hydrogen sources including remnant intracellular water, adsorbed extracellular water, and biomass hydrogen in both non-exchangeable sites and exchangeable sites that are readily mixed with

natural-abundance washing buffers during sample preparation. Protonated sites in biomolecules (e.g., O-H, N-H, S-H, etc.) experience rapid exchange with aqueous wash solutions on the order of picoseconds to minutes (47,48), meaning that anabolically produced O-$^{2}$H, N-$^{2}$H, S-$^{2}$H, etc. bonds would be rapidly overprinted by natural-abundance hydrogen during standard washing procedures (**Fig. 4**). As described in *Materials and Methods*, no stains or probes were applied to the cells in this study. Therefore, the hydrogen dilution factors reported here result solely from sample washing. This significant and persistent isotopic dilution may confound efforts to use deuterium tracers as measures of biosynthesis in nanoSIMS-based studies (10). This problem is compounded at lower-isotopic enrichment, where substantial variability in $^{2}$H/$^{1}$H values results from low $^{2}$H ion counts as well as random variation in which cell subcomponents (e.g., highly exchangeable vs. non-exchangeable) are ablated (10). Our observation that the magnitude of isotopic dilution appears variable across samples (**Fig. 2**) suggests that dilution factors could contribute substantial uncertainty to corrected values. Future work should apply caution when applying dilution factors to back-calculate isotopic abundance, as these can vary widely between the sample preparation and organism (40), an effect that may be pronounced in environmental systems with mixed microbial communities.

A key advantage of Raman-SIP is that the C-H (2800 - 3100 cm$^{-1}$) and C-D (2040 - 2300 cm$^{-1}$) bands report solely non-exchangeable carbon-hydrogen and carbon-deuterium stretching modes associated with mostly lipids, proteins and nucleic acids (8,49). These spectral regions are oblivious to exchangeable bonding environments including O-H, N-H, S-H, etc., as well as remnant water. Raman spectroscopy therefore focuses on biosynthetically produced organic bonds without the confounding effects of remnant water or exchanged biomolecular hydrogen.

281 Deuterium measurements by Raman-SIP appear to exhibit a greater reliability in tracking
282 biosynthetic incorporation of deuterium into cellular biomass.
283

284 ***Future Directions for Raman-SIP***

285 Raman spectroscopy has several advantages for measuring microbial growth rates. First, it is a
286 non-destructive, rapid method that is readily coupled with other techniques such as fluorescence
287 microscopy, fluorescence in situ hybridization (FISH), scanning electron microscopy (SEM), or
288 cell sorting (8,15). A single Raman spectrum takes between seconds to one minute to acquire, and
289 many Raman instruments are equipped with fluorescence modules that can enable visualization of
290 the cells in addition to transmitted or reflected light microscopy. Second, Raman is comparatively
291 accessible relative to nanoSIMS and allows analysis with minimal preparation, making it capable
292 of being deployed directly on many forms of microbial systems including filters from aquatic
293 environments, rock faces, plant material, etc. Third, Raman microspectroscopy has microscale
294 spatial resolution and provides diagnostic information about cellular organic composition. The
295 fingerprint region (200 – 1800 $cm^{-1}$) is routinely used to identify biomolecules (49) as well as
296 differentiate taxa, down to the species/strain level and growth stage (50–52). Fourth, the Raman
297 fingerprint region enables identification of biologically precipitated minerals and the
298 mineralogical/material context of a cell (37,53). Raman SIP with deuterium, specifically, makes
299 identification of individual cell and mineral components in organic-mineral assemblages feasible
300 because the C-D band occupies a typically silent region in inorganic Raman spectra. Co-registered
301 mineral and quantitative cell-activity measurements open the door for novel investigations into the
302 cell-mineral and cell-cell relationships that drive microbial activity in the rock-hosted biosphere

303 (35). Furthermore, measurement of $^{13}C$ and $^{15}N$ enrichment in microbial cells has been
304 demonstrated with Raman (55–59) and the potential exists for the co-registration of multiple stable
305 isotopes at the single-cell level.

306 The main disadvantage of deuterium Raman-SIP is its detection limit. Classical or
307 spontaneous Raman microspectroscopy of microbial cells is limited by low signal intensities,
308 particularly in samples with high autofluorescence (54). A key outcome of our study is the
309 definition of Raman-SIP ranges of quantification. Our study defines the minimum cutoff for
310 quantitative measurement as ~ 7 at. % (**Table 2**), depending on the label strength applied. In the
311 coming years, advancements in Raman technology hold potential for increasing its sensitivity and
312 subsequently improving isotopic measurements. Specifically, surface- or tip-enhanced Raman
313 spectroscopy (SERS or TERS) (50,60–63), stimulated Raman scattering (SRS), resonance Raman
314 spectroscopy, or coherent anti-Stokes Raman spectroscopy (CARS), which are shown to
315 dramatically improve acquisition times, and enhance signal, could be applied to determine isotopic
316 enrichments (55,56,60,64–69). However, at present, robust validation of these methods for
317 deuterium SIP is required (**Supplemental Text, Supplemental Fig. S4 – S5**).

318 Our results point to Raman microspectroscopy being a powerful tool for conducting SIP,
319 especially where complex environmental matrices may complicate bulk-omics or other single-cell
320 approaches. For the benefit of future researchers, we designed an interactive graphical user
321 interface (GUI), *Shiny R-SIP*, that allows users to implement our SIP model and optimize their
322 experiments by considering how the relevant sources of uncertainty impact the design of a Raman-
323 SIP experiment (*Supplementary Data* or online: https://apps.kopflab.org/login with login
324 credentials username: *shiny-rSIP*, password: *public-access*). The GUI allows users to adjust

parameters of label strength, incubation time, and water hydrogen assimilation efficiency, as well associated uncertainties in these terms, in order to design effective SIP experiments. The parameters we define in our microbial growth model are specific to the study organisms used and our Raman instrument: they are intended to provide reasonable estimates of uncertainty that may be encountered. Users of this GUI are encouraged to define their own uncertainty terms by constraining the technical variation in individual CD% measurements inherent to their Raman instrument. For samples where microbial growth may exhibit large variation, we suggest users consider multiple incubation times (or sub-sampling efforts) to effectively capture a wide range of biomass growth rates in experiments targeting natural microbial communities, while also quantifying their threshold of tracer saturation as an upper-limit of growth-rate quantification.

## Conclusions

In this work, we provide the basis for the quantitative measurement of single-cell microbial growth rates via Raman-SIP. We develop hydrogen isotope calibrations for two organisms, *T. hydrogeniphilus* (sulfate-reducing bacterium) and *M. NSHQ04* (methanogenic archaeon). These calibrations validate the utility of Raman microspectroscopy as a method for measuring microbial $^{2}H/H$ enrichment. Applying our Raman-derived isotopic calibration to a model of microbial growth, we define ranges of quantification for Raman SIP experiments where single-cell growth rates can be sensitively distinguished. We find that with reasonable (20 - 40 at. % $^{2}H_2O$) isotopic label strengths and incubation times, Raman-SIP can capture a wide array of microbial generation times, with this range being defined by the parameters of the SIP experiment. These ranges of quantification can guide the design and interpretation of SIP experiments where Raman is used to

track cellular $^2H$ incorporation. Finally, we observe that hydrogen isotopic values derived from nanoSIMS suffer from severe dilution that may complicate the use of nanoSIMS for quantifying cellular $^2H$ uptake. In conclusion, this work provides a robust framework for applying deuterium Raman-SIP to spatially resolved, quantitative investigations of microbial activity in environmental and model systems.

# Materials and Methods

### *Microorganisms and Growth Conditions*

We cultivated *Thermodesulfovibrio hydrogeniphilus* (43) and *Methanobacterium NSHQ04* (44), in media containing 0%, 10%, 20%, 30%, 40%, or 50% $^2H_2O$ (0% = local ultra-pure water which contains ~140ppm $^2H_2O$ naturally). Base media (described below) were modified with different percentages (vol/vol) of $^2H_2O$ [Cambridge Isotope Laboratories], depending on the final isotopic enrichment desired for the experiment. All cultures were grown in the dark in anaerobic 60 ml serum vials containing 25 ml of growth medium.

*Thermodesulfovibrio hydrogeniphilus* HBr5$^T$ (DSM 18151) (43), a sulfate reducing bacterium, was obtained from the Deutsche Sammlung von Mikroorganismen und Zellkulturen (DSMZ). It was grown in a modified DSM 641 medium that contained (per liter): 1.0g $NH_4Cl$, 2.0g $Na_2SO_4$, 1.0g $Na_2S_2O_3x5H_2O$, 1.0g $MgSO_4x7H_2O$, 0.1g $CaCl_2x2H_2O$, 0.5g $KH_2PO_4$, 2.0g $NaHCO_3$, 1ml trace element solution SL-10, 1ml selenite-tungstate solution, 1g yeast extract, 0.5ml sodium resazurin (0.1% wt/vol), 0.2g sodium acetate, 10ml 141 vitamin solution, and 0.1g $Na_2S$ x $9H_2O$. The headspace was flushed and over-pressurized with 1 bar $H_2$:$CO_2$ (80:20).

367 *Methanobacterium NSHQ04* (44) is a methanogenic archaeon enriched from groundwater
368 isolated from the Samail ophiolite in Oman. The culture was grown in a synthetic site water
369 (NSHQ04) medium (44) containing (per liter): 420mg NaCl, 683mg $CaCl_2x2H_2O$, 1.2mg $H_4SiO_4$,
370 1.7mg NaBr, 60mg $MgCl_2x6H_2O$, 100mg $NH_4Cl$, 10 ml 141 trace elements, 10ml 141 vitamins,
371 0.5ml sodium resazurin (0.1 wt/vol), 20ml antibiotic cocktail [containing per 100ml MilliQ water,
372 500mg penicillin G, 500mg streptomycin, 500ul ampicillin (10mg/ml stock)], 10ml $KH_2PO_4$ (1.1
373 wt/vol), 4ml yeast extract (5% wt/vol), 2ml $Fe(NH_4)_2(SO_4)_2$ (0.2% w/v), 10ml sodium formate
374 (100mM), 10ml cysteine-HCl (2.5% w/v), and 10ml $Na_2S$ (2.5% w/v). The headspace was flushed
375 and over-pressurized with 2 bar $H_2$:$N_2$ (5:95).

376 Cultures of *T. hydrogeniphilus* and *M. NSHQ04* were incubated in forced-air incubators at
377 65°C and 40°C, respectively. Cultures were transferred three times into media of identical
378 deuterium enrichment. Before each transfer, cultures were grown to stationary phase, which was
379 reached in 3-4 days for *T. hydrogeniphilus* and 12-14 days for *Methanobacterium NSHQ04*. This
380 ensured that the cells measured were at or near isotopic equilibrium with their respective growth
381 water, offset by $a_w$. After the third transfer, 1ml of each culture was harvested and fixed by addition
382 of paraformaldehyde to a final concentration of 2% (vol/vol). Fixed cells were washed by
383 centrifugation in successively dilute phosphate-buffered saline (PBS) of rinses [1X, 1%, 0.1%, and
384 0.01% (vol/vol) PBS) to ensure the removal of excess salts and fixative. PBS was composed of
385 Dulbecco's formula: KCl 200 mg/L, $KH_2PO_4$ 200 mg/L, NaCl 8000 mg/L, $Na_2HPO_4$ 1150 mg/L.
386 After the final wash, cells were resuspended in 50µl of 0.01% (vol/vol) PBS.
387

### *Sample Preparation*

Sample coupons were prepared by raster engraving of aluminum-coated glass slides (Deposition Research Lab Inc.) with an Epilog Mini 24 $CO_2$ laser machine operating at 80 W laser power, 10% etching speed, to create a 3 x 6 grid. These etchings were used to manually break the glass slide, producing 7mm$^2$ coupons that are compatible with both Raman and nanoSIMS sample mounts. Aluminum coupons were used instead of silicon wafers (typically used for nanoSIMS studies) because silicon exhibits a large peak at 520 cm$^{-1}$ in the Raman spectrum. All coupons were sterilized and rendered organic-clean by combustion for 8 hours at 450°C in a muffle furnace. 5µl of fixed and washed cells was spotted on individual coupons and allowed to air-dry.

### *Raman Spectroscopy, Fitting, and SIP Calculations*

Raman spectroscopy was conducted at the Raman Microspectroscopy Laboratory, Department of Geological Sciences, University of Colorado-Boulder (RRID:SCR_019305) on a Horiba LabRAM HR Evolution Raman spectrometer equipped with a 100mW 532 nm excitation laser. The laser was focused with a 100X (NA = 0.90) air objective lens, resulting in a spot size of ~1µm. Single-cell spectra were captured in the 200-3150 cm$^{-1}$ range using 100% laser power (2.55 mW) over 2 acquisitions of 45 seconds. A 100 µm confocal pinhole and 600 lines/mm diffraction grating were used, resulting in a spectral resolution of ~ 4.5 cm$^{-1}$. Duplicate acquisitions were averaged to remove noise and cosmic ray spikes. Spectra were baseline-subtracted using a polynomial fit in LabSpec 6 (Horiba Scientific). Fitting of bands in the 1800 - 3150 cm$^{-1}$ region was performed using Gaussian-Lorentzian curve fitting algorithms to integrate C-D (2040 – 2300 cm$^{-1}$) and C-H (2800 – 3100 cm$^{-1}$) bands. Raman-derived $^2F$ was determined by calculating the CD% value of

each spectrum: $^2F = CD\% = CD / (CH + CD) \times 100\%$ where CD and CH are the areas of the C-D and C-H bands, respectively.

To correlate Raman spectra with nanoSIMS data, extensive context maps of the sample coupons were acquired using reflected light microscopy on the Raman instrument. Before cell spotting, fiducial markings were etched into the aluminum coupon surface with a Leica LMD7000 microdissection system.

As described in *Results and Discussion*, modeling of growth rate was carried out with **Eq. 1 – 3.** (3,14). Using these formulae, we modeled $\mu$ across a range of $F_L$, $t$, and $a_w$. We define an acceptable cutoff using a relative error term defined as the fraction of uncertainty in calculated growth rate over the growth rate itself ($\sigma_\mu / \mu$) where quantifiable growth rate is where Relative Error = $(\sigma_\mu / \mu) \times 100\ \% < 50\%$ **(Fig. 3)**.

The value of the water hydrogen assimilation constant ($a_w$) was determined for both organisms from the slopes of the linear regression relating $^2F_{biomass}$ vs. $^2F_{water}$. This value, $a_w = X_w \times \alpha_{biomass/w}$, corresponds to the isotopic offset between microbial biomass relative to its growth water. This term includes both $X_w$, the mole fraction of lipid H sourced from growth water, and $\alpha_{biomass/w}$, the isotopic fractionation between whole-cell biomass and growth water (21).

### *Nanoscale Secondary Ion Mass Spectrometry*

Samples were analyzed with a CAMECA NanoSIMS 50L (CAMECA, Gennevilliers, France) housed in the Caltech Microanalysis Center at the California Institute of Technology. Before, analysis, cells were sputter-coated with 25nm of Au. Cells were analyzed using a 2.5 pA primary Cs+ beam current, and a presputter time of 6 – 20 minutes depending on the size of the raster area.

Two masses were collected in parallel ($^{1}H^{-}$, $^{2}H^{-}$) using electron multipliers. Individual samples were identified using the NanoSIMS CCD camera and correlated with Raman-measurements using previously generated image maps. For all analyses, at least two frames were collected. All ion images were recorded at 512 x 512-pixel area. Single-cell isotope values were quantified using a custom script (see *Data Availability*) relying on the *sims* Python library (https://github.com/zanpeeters/sims). Cell areas were manually defined using the GNU Image Manipulation Program (GIMP). Isotope ratios ($^{2}R$) were converted to fractional abundances ($^{2}F$) with the relations: $^{2}F = {}^{2}R / (1 + {}^{2}R)$ and $^{2}R = {}^{2}H / {}^{1}H$, where $^{1}H$ and $^{2}H$ represent total ion counts in detectors EM1 and EM2, respectively, averaged across a cell area. Additionally, a deadtime correction (70) was applied:

$$N = \frac{N_m}{1 - N_m \cdot \tau / T} \qquad \text{(Eq. 4)}$$

where $N$ is the real number of secondary ions, $N_m$ is the number of secondary ions measured, $\tau$ is deadtime (in seconds) and $T$ is dwell time (seconds per pixel). This instrument's detector deadtime was 44 ns. Deadtime correction had a negligible effect on isotopic values (**Supplementary Text, Supplementary Fig. S7**).

## Author Contributions

Tristan Caro and Srishti Kashyap designed the study and performed the experiments. Tristan Caro, Srishti Kashyap, Claudia Chen, and George Brown analyzed the data. Alexis Templeton and

Sebastian Kopf provided financial support for the study. Tristan Caro and Sebastian Kopf designed the GUI. Alexis Templeton and Sebastian Kopf contributed to the design of the study and interpretation of its findings. Tristan Caro wrote the manuscript with input from all authors.

## Data Availability

Raw data and analysis scripts used to process data and generate visualizations are available at https://github.com/tacaro/Caro-et-al-Raman-SIP. The interactive GUI referenced in this manuscript is available at https://apps.kopflab.org/login with login username *shiny-rSIP* and password *public-access.* In addition, a copy can be downloaded for offline use from the manuscript GitHub repository.

## Acknowledgements

The authors would like to thank the University of Colorado Boulder, Department of Geological Sciences for support of this study. This work was also supported by a NASA Exobiology Program grant to Alexis Templeton (80NSSC21K0489) and an Army Research Office grant to Sebastian Kopf (W911NF2120119 / 78484-LS). The authors sincerely thank Yunbin Guan of the Caltech Microanalysis Center for expertise with nanoSIMS measurements. We thank Eric Ellison of the CU Boulder Raman Microspectroscopy Laboratory (RRID:SCR_019305) for assistance with Raman measurements and data analysis. We extend sincere thanks to John Magyar for helpful discussions during the design of this study. We credit Dan Utter for assistance with nanoSIMS data processing and initial drafting of the nanoSIMS data extraction script. We thank Rebecca

Wipfler for assistance with laser microdissection microscopy and coupon etching. Tristan Caro was supported by a National Science Foundation Graduate Research Fellowship and through the BioFrontiers Institute of the University of Colorado Boulder. Claudia Chen and George Brown were supported by the Laboratory for Interdisciplinary Statistical Analysis at the University of Colorado Boulder. The Laboratory for Interdisciplinary Statistical Analysis at the University of Colorado Boulder is supported by National Science Foundation Grant No. 1955109.

## Figures and Tables

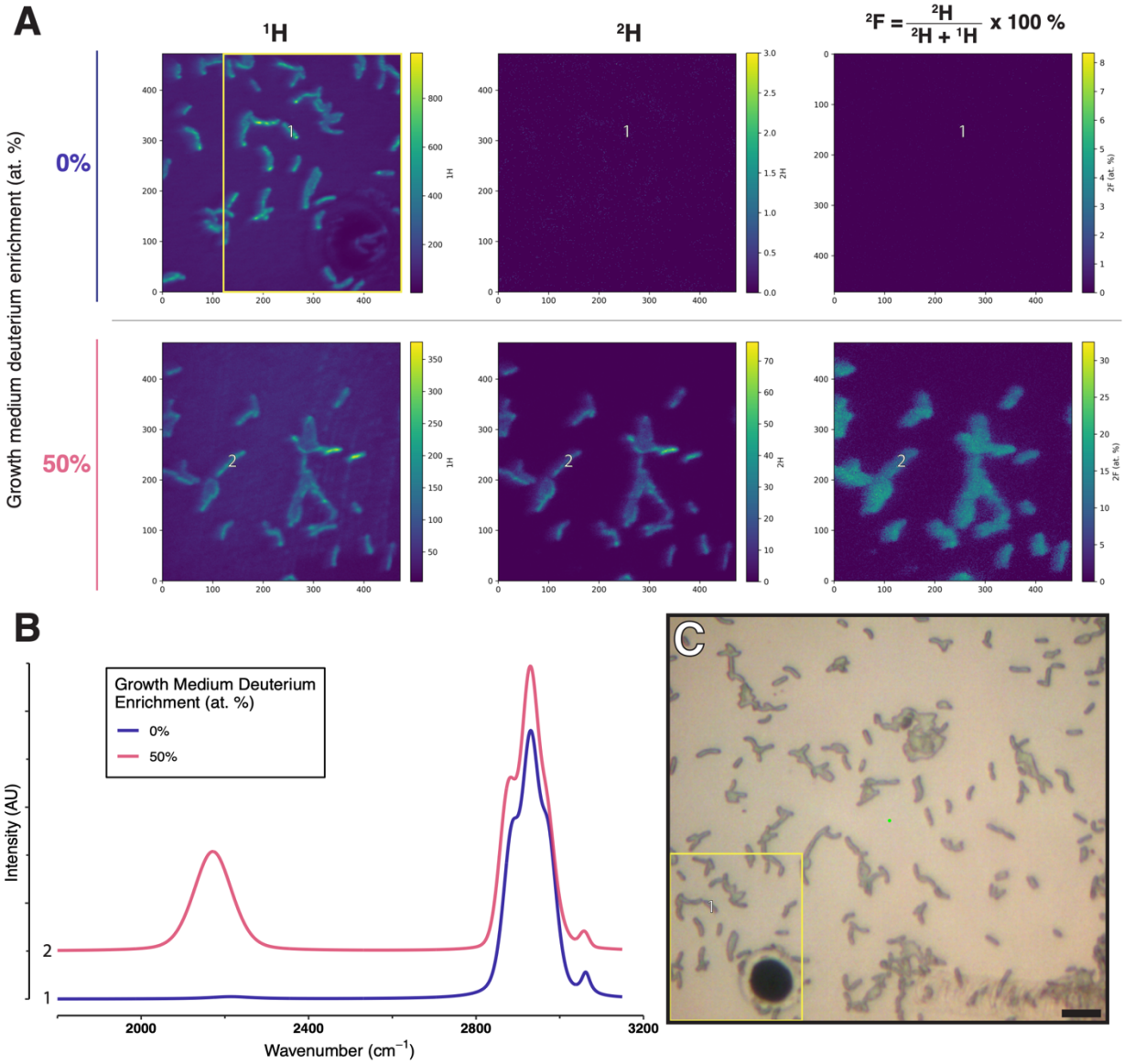


**Figure 1: Representative Raman and nanoSIMS data collected in this study.**

Across all panels data from two representative cells, "1" and "2", are noted. Representative nanoSIMS isotopic images of are shown in **Panel A**, with pixel counts labeled on the x and y axes. From left to right, the pixel intensity in each panel corresponds to direct ion counts for $^1H^-$, $^2H^-$, and the fractional abundance

of deuterium ($^2F$), respectively. The top row shows cells grown in 0% $^2H_2O$ (natural abundance); the bottom row displays cells grown in 50 at. % $^2H_2O$. Representative single-cell fitted Raman spectra are shown in **Panel B**, with the characteristic C-H band between 2800 and 3000 $cm^{-1}$ clearly visible. For cells grown in deuterated media (Cell 2), the C-D band emerges between 2040 and 2300 $cm^{-1}$. **Panel C** displays a typical micrograph captured through a confocal Raman microspectroscope. The scale bar represents 2µm. Cells in all panels represent *T. hydrogeniphilus.* The yellow boxes in the top-left facet of Panel A, and Panel C, represent a correlated region imaged with nanoSIMS and Raman (reflected light), respectively.

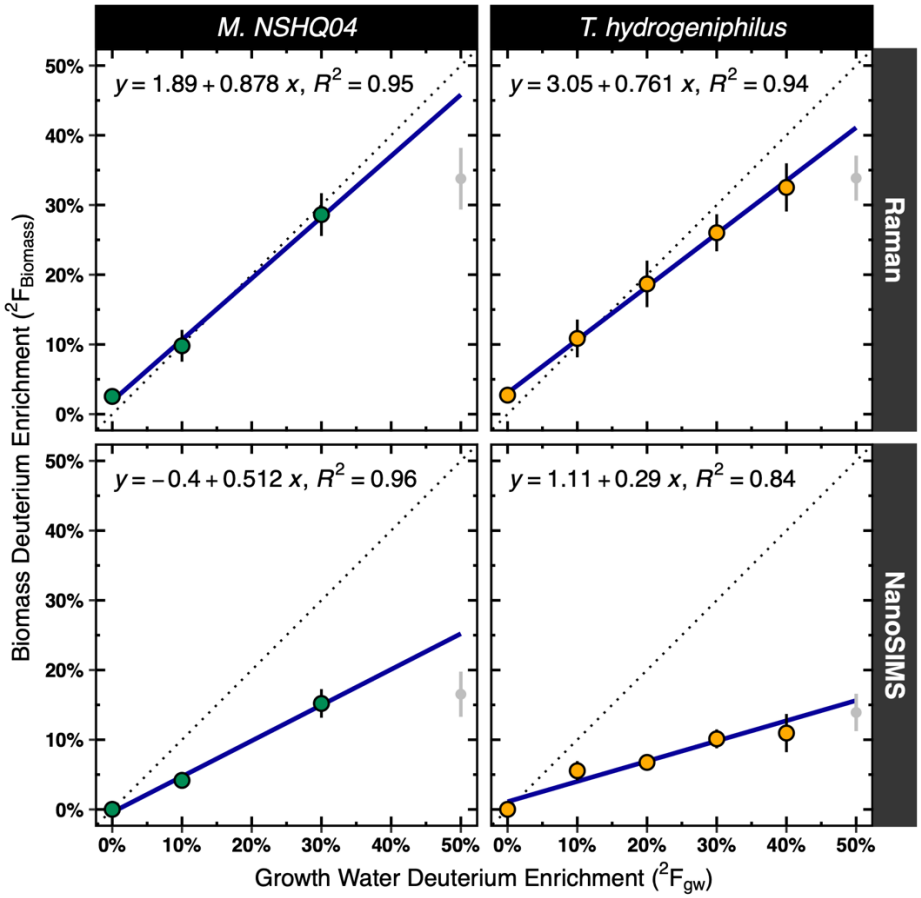


494

495 **Figure 2: Hydrogen isotope calibrations relating growth water and biomass $^2$H content.**

496 Individual measurements of single-cell biomass deuterium enrichment ($^2F_{biomass}$) conducted with Raman
497 spectroscopy (top panels) or nanoSIMS (bottom panels) are plotted against the corresponding deuterium
498 content of the microbial growth media ($^2F_{gw}$). The dotted line indicates the 1:1 line; the solid blue line
499 represents the line of best fit whose equation is noted in each panel. Points and error bars displayed are
500 mean and standard deviation of biomass deuterium enrichment, respectively. Note that the linear models
501 displayed in each panel are calculated only with data between deuterium enrichments of 0 – 40 at. % to
502 ensure that these models are not affected by the toxicity effects observed at 50 at. % label isotopic
503 enrichment (point intervals in gray).

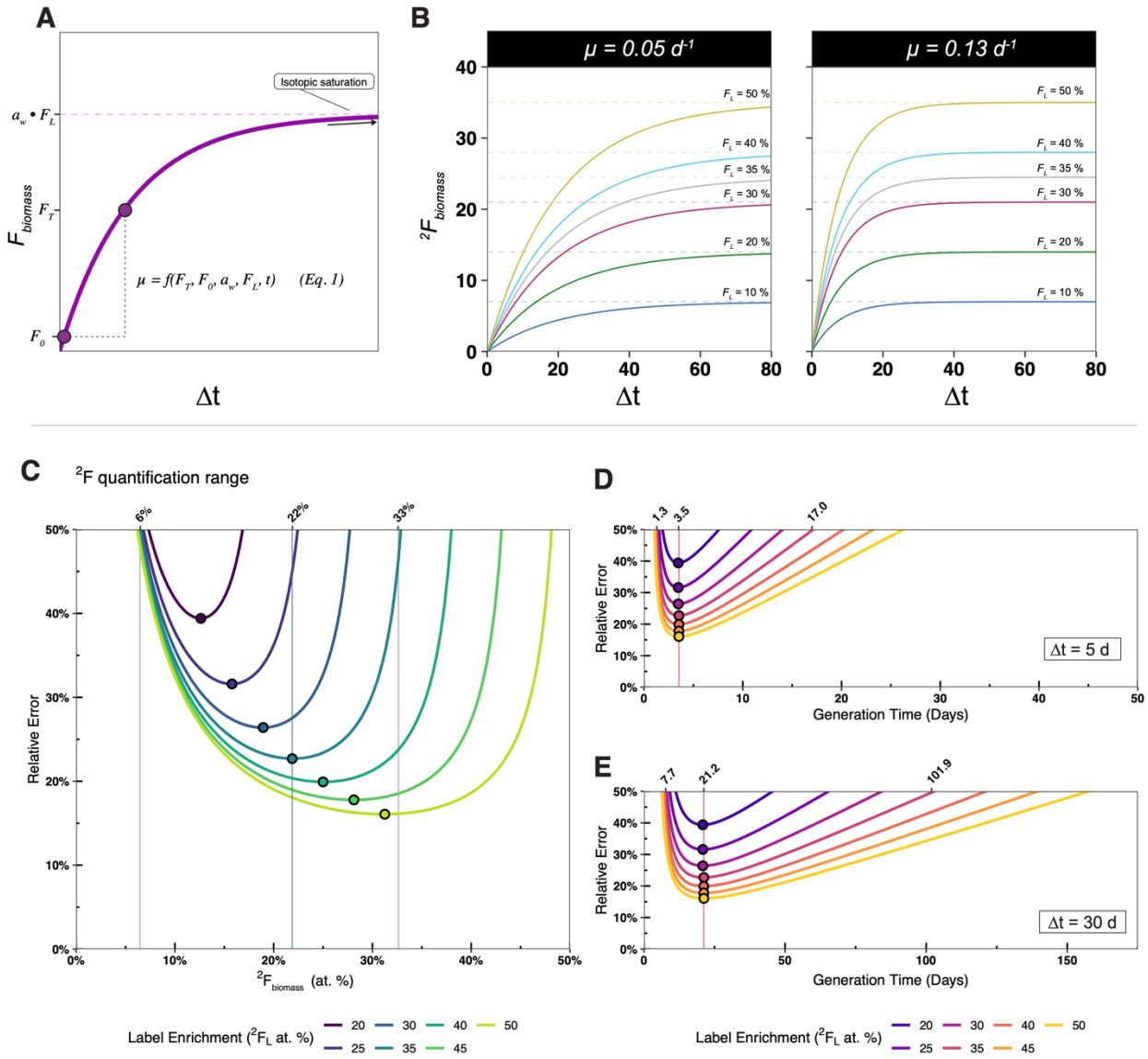


504

505 **Figure 3: Modeling of microbial growth in the presence of enriched isotopic label (A, B) and**
506 **associated error in biomass $^2$F quantification (C) and growth rate/generation time (D, E).**
507 A schematic figure (**Panel A**) visualizes how microbial growth rate is calculated as a function of biomass
508 isotopic enrichment ($F_T$), label strength ($F_L$), incubation time ($t$), and water assimilation efficiency constant
509 ($a_w$) **(Eq. 1)**. Similarly, **Panel B** displays example output of the microbial growth model, where $a_w$ = 0.7.

Isotopic enrichment increases as a function of time but depends upon isotopic label strength ($F_L$) and growth rate ($\mu$, noted above each plot). In **Panels C-E**, we display quantification ranges where relative error in the growth rate measurement is < 50% of the growth rate itself (Relative Error = $\sigma_\mu / \mu \times 100\%$ where μ is apparent growth rate). In **Panel C,** relative error is plotted against biomass deuterium enrichment ($^2F_{biomass}$) for label strengths $^2F_L$ ranging from 20-50 at. %. Plotted points indicate the of minimum error for each isotopic label. Along the top axis of **Panel C**, the lower limit, error optimum, and upper limit of quantification, are noted, for the isotopic label strength of $^2F_L$ = 35 at. %. The key results from **Panel C** are summarized in **Table 2.** In **Panels D** and **E,** relative error is plotted against biomass generation times in the context of a simulated SIP incubation. In these examples, the incubation times of 5 days (**Panel D**) and 30 days (**Panel E**) are chosen. Along the top axes of **Panels D** and **E**, the minimum, optimum, and maximum quantifiable generation times are noted for the isotopic tracer strength of $^2F_L$ = 35 at. %. These generation times correspond to the limits of quantification and optima noted in Panel A.

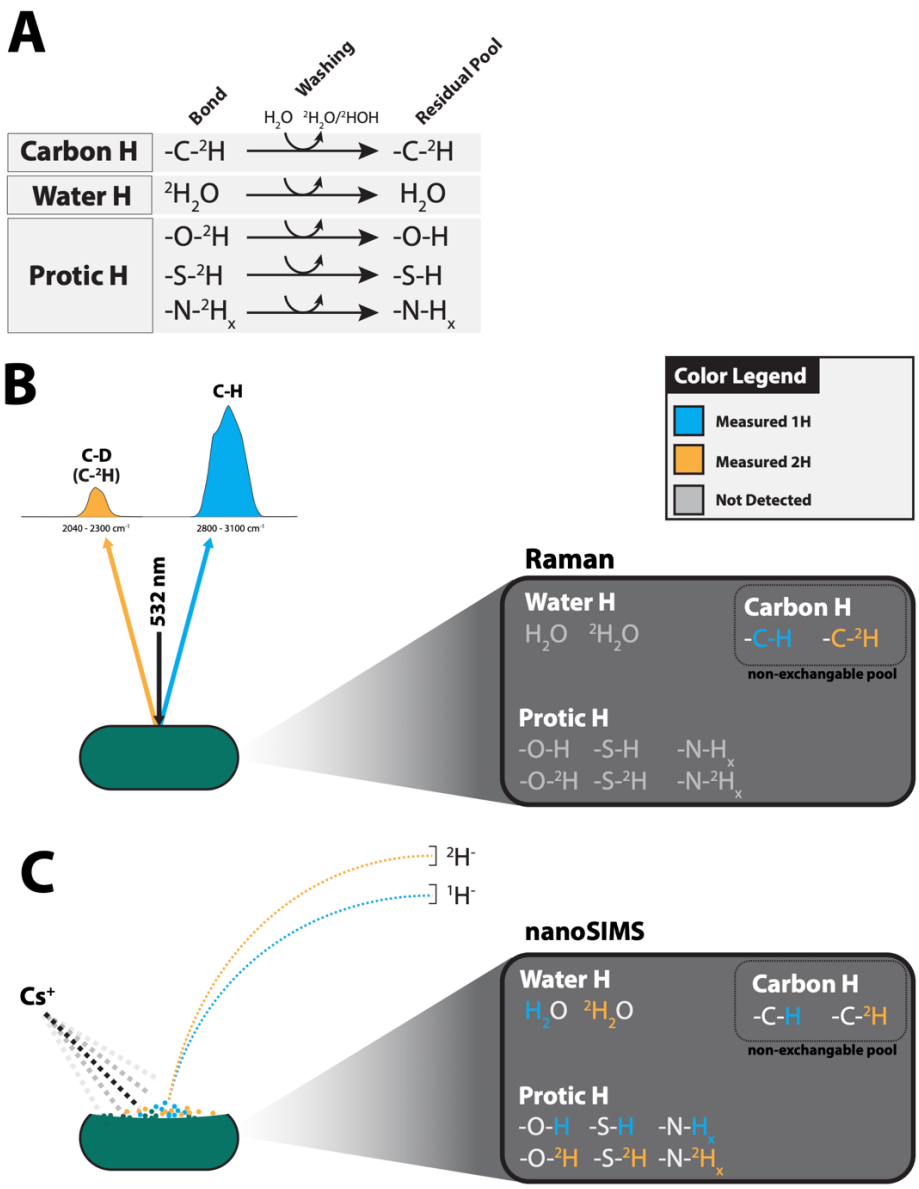


**Figure 4. Schematic diagram showing the dilution of $^2$H/H isotopic signal due to sample preparation, and how Raman and nanoSIMS measure different pools of biomass $^2$H/H.** **(A)** The original pool of deuterated cell mass is biosynthesized, sourcing $^2$H from the growth medium. During sample washing, hydrogen in exchangeable, or "protic" bonding environments rapidly exchange with wash solutions, leaving a diluted residual pool of $^2$H/H. Carbon-hydrogen and carbon-deuterium bonds

are not affected by this dilution effect, as $^{2}H/H$ in these bonds do not exchange during washing. **(B)** Within the C-H and C-D (C-$^{2}H$) wavenumber regions, Raman is only sensitive to carbon-hydrogen and carbon-deuterium bonds, which are not affected by dilution due to washing, whereas **(C)** nanoSIMS ostensibly measures all pools of $^{2}H/H$, including those affected by dilution.

**Table 1. Results and statistical summary of the isotopic calibration**.

Here we summarize key outputs of our analyses: (A) analytical uncertainty in biomass measurements across growth water isotopic compositions ($^2F_{gw}$), (B) Linear models relating the isotopic composition of biomass ($^2F_{biomass}$) to that of growth water ($^2F_{gw}$), (C) Water hydrogen assimilation efficiency factors ($a_w$) derived from the hydrogen isotopic calibration, with associated standard error, (D) Assessment of correlation between biomass isotopic values estimated with Raman spectroscopy ($^2F_{Raman}$)and nanoSIMS ($^2F_{nanoSIMS}$) (**Supplementary Fig. S2, S3**).

| | **Raman** | **nanoSIMS** |
|---|---|---|
| **(A) Analytical Uncertainty in Cellular $^2F$ (SD) (at. %)** | | |
| $^2F_{gw}$= 0% (SD of the method blank) | 1.13 | 0.01 |
| $^2F_{gw}$ = 10% | 2.56 | 1.24 |
| $^2F_{gw}$ = 20% | 3.34 | 1.04 |
| $^2F_{gw}$ = 30% | 3.07 | 2.95 |
| $^2F_{gw}$ = 40% | 3.46 | 2.74 |
| $^2F_{gw}$ = 50% | 3.78 | 3.20 |
| Mean SD across all conditions | 2.89 | 1.86 |
| **(B) Hydrogen Isotope Calibration Models** *where: $y = {}^2F_{Biomass}$, $x = {}^2F_{gw}$* | | |

| | | |
|---|---|---|
| *T. hydrogeniphilus* | y = 0.761x + 3.05<br>$R^2$ = 0.94 | y = 0.29x + 1.11<br>$R^2$ = 0.84 |
| *M. NSHQ04* | y = 0.878x + 1.89<br>$R^2$ = 0.95 | y = 0.512x – 0.40<br>$R^2$ = 0.96 |
| **(C) Water hydrogen assimilation efficiency**<br>$a_w \pm SE$ | | |
| *T. hydrogeniphilus* | 0.761 ± 0.014 | 0.290 ± 0.009 |
| *M. NSHQ04* | 0.878 ± 0.020 | 0.512 ± 0.010 |
| **(D) Correlative Statistics** | | |
| Linear model equation<br>*where:*<br>$y = {}^2F_{nanoSIMS}$<br>$x = {}^2F_{Raman}$<br>(Supplementary Text, Supplementary Fig. S2-S3) | y = 0.439x – 0.3617<br>Slope SE = 0.01<br>Intercept SE = 0.24 | |
| RMSE (at. %) | 2.52 | |

533

**Table 2: Range of Quantification for Raman-derived (CD%-based) measurements of single-cell deuterium content (Fig. 3C).**

The optimum value represents the $^{2}F_{biomass}$ value at which relative error in growth rate calculation is minimized. The lower and upper limits of quantification represent where relative error of growth rate calculation exceeds 50%.

| Isotopic label strength ($^{2}F_{L}$ at. %) | Lower limit of quantification ($^{2}F_{biomass}$ at. %) | Optimum ($^{2}F_{biomass}$ at. %) | Upper limit of quantification ($^{2}F_{biomass}$ at. %) |
|---|---|---|---|
| 20 | 7.4 | 12.6 | 16.7 |
| 25 | 6.8 | 15.8 | 22.4 |
| 30 | 6.6 | 18.9 | 27.7 |
| 35 | 6.4 | 21.8 | 32.6 |
| 40 | 6.4 | 25.0 | 37.7 |
| 45 | 6.3 | 28.1 | 42.8 |
| 50 | 6.2 | 31.3 | 48.0 |

534

## References

1. Dumont MG, Murrell JC. Stable isotope probing — linking microbial identity to function. Nat Rev Microbiol. 2005 Jun;3(6):499–504.

2. Hungate BA, Mau RL, Schwartz E, Caporaso JG, Dijkstra P, van Gestel N, et al. Quantitative Microbial Ecology through Stable Isotope Probing. Appl Environ Microbiol. 2015 Nov 1;81(21):7570–81.

3. Caro TA, McFarlin J, Jech S, Fierer N, Kopf S. Hydrogen stable isotope probing of lipids demonstrates slow rates of microbial growth in soil. Proc Natl Acad Sci. 2023 Apr 18;120(16):e2211625120.

4. Trembath-Reichert E, Morono Y, Ijiri A, Hoshino T, Dawson KS, Inagaki F, et al. Methyl-compound use and slow growth characterize microbial life in 2-km-deep subseafloor coal and shale beds. Proc Natl Acad Sci. 2017 Oct 31;114(44):E9206–15.

5. Cui L, Yang K, Zhu YG. Stable Isotope-Labeled Single-Cell Raman Spectroscopy Revealing Function and Activity of Environmental Microbes. In: Dumont MG, Hernández García M, editors. Stable Isotope Probing: Methods and Protocols [Internet]. New York, NY: Springer; 2019 [cited 2022 Mar 28]. p. 95–107. (Methods in Molecular Biology). Available from: https://doi.org/10.1007/978-1-4939-9721-3_8

6. Eichorst SA, Strasser F, Woyke T, Schintlmeister A, Wagner M, Woebken D. Advancements in the application of NanoSIMS and Raman microspectroscopy to investigate the activity of

554 microbial cells in soils. FEMS Microbiol Ecol [Internet]. 2015 Oct 1 [cited 2021 Feb
555 2];91(fiv106). Available from: https://doi.org/10.1093/femsec/fiv106

556 7. Trembath-Reichert E, Shah Walter SR, Ortiz MAF, Carter PD, Girguis PR, Huber JA. Multiple
557 carbon incorporation strategies support microbial survival in cold subseafloor crustal fluids.
558 Sci Adv. 2021 Apr;7(18):eabg0153.

559 8. Berry D, Mader E, Lee TK, Woebken D, Wang Y, Zhu D, et al. Tracking heavy water (D2O)
560 incorporation for identifying and sorting active microbial cells. Proc Natl Acad Sci. 2015 Jan
561 13;112(2):E194–203.

562 9. Wegener G, Kellermann MY, Elvert M. Tracking activity and function of microorganisms by
563 stable isotope probing of membrane lipids. Curr Opin Biotechnol. 2016 Oct 1;41:43–52.

564 10. Kopf SH, McGlynn SE, Green-Saxena A, Guan Y, Newman DK, Orphan VJ. Heavy water
565 and 15N labelling with NanoSIMS analysis reveals growth rate-dependent metabolic
566 heterogeneity in chemostats. Environ Microbiol. 2015;17(7):2542–56.

567 11. Koch BJ, McHugh TA, Hayer M, Schwartz E, Blazewicz SJ, Dijkstra P, et al. Estimating
568 taxon-specific population dynamics in diverse microbial communities. Ecosphere.
569 2018;9(1):e02090.

570 12. Li J, Mau RL, Dijkstra P, Koch BJ, Schwartz E, Liu XJA, et al. Predictive genomic traits for
571 bacterial growth in culture versus actual growth in soil. ISME J. 2019 Sep;13(9):2162–72.

13. Coskun ÖK, Özen V, Wankel SD, Orsi WD. Quantifying population-specific growth in benthic bacterial communities under low oxygen using H 2 18 O. ISME J. 2019 Jun;13(6):1546–59.

14. Kopf SH, Sessions AL, Cowley ES, Reyes C, Sambeek LV, Hu Y, et al. Trace incorporation of heavy water reveals slow and heterogeneous pathogen growth rates in cystic fibrosis sputum. Proc Natl Acad Sci. 2016 Jan 12;113(2):E110–6.

15. Schaible GA, Kohtz AJ, Cliff J, Hatzenpichler R. Correlative SIP-FISH-Raman-SEM-NanoSIMS links identity, morphology, biochemistry, and physiology of environmental microbes. ISME Commun. 2022 Jun 30;2(1):1–10.

16. Wegener G, Bausch M, Holler T, Thang NM, Mollar XP, Kellermann MY, et al. Assessing sub-seafloor microbial activity by combined stable isotope probing with deuterated water and 13C-bicarbonate. Environ Microbiol. 2012;14(6):1517–27.

17. Kellermann MY, Wegener G, Elvert M, Yoshinaga MY, Lin YS, Holler T, et al. Autotrophy as a predominant mode of carbon fixation in anaerobic methane-oxidizing microbial communities. Proc Natl Acad Sci. 2012 Nov 20;109(47):19321–6.

18. Morono Y, Terada T, Nishizawa M, Ito M, Hillion F, Takahata N, et al. Carbon and nitrogen assimilation in deep subseafloor microbial cells. Proc Natl Acad Sci. 2011 Nov 8;108(45):18295–300.

19. Damoglou AP, Dawes EA. Studies on the lipid content and phosphate requirement of glucose- and acetate-grown Escherichia coli. Biochem J. 1968 Dec 1;110(4):775–81.

20. Neidhardt FC, editor. Escherichia coli and Salmonella typhimurium: cellular and molecular biology. Washington, D.C: American Society for Microbiology; 1987. 2 p.

21. Zhang X, Gillespie AL, Sessions AL. Large D/H variations in bacterial lipids reflect central metabolic pathways. Proc Natl Acad Sci. 2009 Aug 4;106(31):12580–6.

22. Sessions AL, Jahnke LL, Schimmelmann A, Hayes JM. Hydrogen isotope fractionation in lipids of the methane-oxidizing bacterium Methylococcus capsulatus. Geochim Cosmochim Acta. 2002 Nov 15;66(22):3955–69.

23. Valentine DL, Sessions AL, Tyler SC, Chidthaisong A. Hydrogen isotope fractionation during H2/CO2 acetogenesis: hydrogen utilization efficiency and the origin of lipid-bound hydrogen. Geobiology. 2004;2(3):179–88.

24. Leavitt WD, Kopf SH, Weber Y, Chiu B, McFarlin JM, Elling FJ, et al. Controls on the hydrogen isotope composition of tetraether lipids in an autotrophic ammonia-oxidizing marine archaeon. Geochim Cosmochim Acta. 2023 Jul 1;352:194–210.

25. Wijker RS, Sessions AL, Fuhrer T, Phan M. 2H/1H variation in microbial lipids is controlled by NADPH metabolism. Proc Natl Acad Sci. 2019 Jun 18;116(25):12173–82.

26. Boetius A, Ravenschlag K, Schubert CJ, Rickert D, Widdel F, Gieseke A, et al. A marine microbial consortium apparently mediating anaerobic oxidation of methane. Nature. 2000 Oct;407(6804):623–6.

27. Cordero OX, Ventouras LA, DeLong EF, Polz MF. Public good dynamics drive evolution of iron acquisition strategies in natural bacterioplankton populations. Proc Natl Acad Sci. 2012 Dec 4;109(49):20059–64.

28. Marlow J, Spietz R, Kim KY, Ellisman M, Girguis P, Hatzenpichler R. Spatially resolved correlative microscopy and microbial identification reveal dynamic depth- and mineral-dependent anabolic activity in salt marsh sediment. Environ Microbiol. 2021;23(8):4756–77.

29. Védère C, Vieublé Gonod L, Nunan N, Chenu C. Opportunities and limits in imaging microorganisms and their activities in soil microhabitats. Soil Biol Biochem. 2022 Nov 1;174:108807.

30. Sokol NW, Slessarev E, Marschmann GL, Nicolas A, Blazewicz SJ, Brodie EL, et al. Life and death in the soil microbiome: how ecological processes influence biogeochemistry. Nat Rev Microbiol. 2022 Feb 28;1–16.

31. Ebrahimi A, Schwartzman J, Cordero OX. Cooperation and spatial self-organization determine rate and efficiency of particulate organic matter degradation in marine bacteria. Proc Natl Acad Sci. 2019 Nov 12;116(46):23309–16.

32. Kirchman DL. Growth Rates of Microbes in the Oceans. Annu Rev Mar Sci. 2016;8(1):285–309.

33. Grossart HP, Kiørboe T, Tang K, Ploug H. Bacterial Colonization of Particles: Growth and Interactions. Appl Environ Microbiol. 2003 Jun;69(6):3500–9.

34. Casar CP, Kruger BR, Flynn TM, Masterson AL, Momper LM, Osburn MR. Mineral-hosted biofilm communities in the continental deep subsurface, Deep Mine Microbial Observatory, SD, USA. Geobiology. 2020;18(4):508–22.

35. Templeton AS, Caro TA. The Rock-Hosted Biosphere. Annu Rev Earth Planet Sci. 2023;51(1):493–519.

36. Woebken D, Burow LC, Behnam F, Mayali X, Schintlmeister A, Fleming ED, et al. Revisiting N2 fixation in Guerrero Negro intertidal microbial mats with a functional single-cell approach. ISME J. 2015 Feb;9(2):485–96.

37. Suzuki Y, Yamashita S, Kouduka M, Ao Y, Mukai H, Mitsunobu S, et al. Deep microbial proliferation at the basalt interface in 33.5–104 million-year-old oceanic crust. Commun Biol. 2020 Apr 2;3(1):1–9.

38. Dekas AE, Parada AE, Mayali X, Fuhrman JA, Wollard J, Weber PK, et al. Characterizing Chemoautotrophy and Heterotrophy in Marine Archaea and Bacteria With Single-Cell Multi-isotope NanoSIP. Front Microbiol [Internet]. 2019 [cited 2023 Jun 7];10. Available from: https://www.frontiersin.org/articles/10.3389/fmicb.2019.02682

39. Arandia-Gorostidi N, Parada AE, Dekas AE. Single-cell view of deep-sea microbial activity and intracommunity heterogeneity. ISME J. 2022 Oct 6;1–11.

40. Meyer NR, Fortney JL, Dekas AE. NanoSIMS sample preparation decreases isotope enrichment: magnitude, variability and implications for single-cell rates of microbial activity. Environ Microbiol. 2021;23(1):81–98.

41. Stryhanyuk H, Calabrese F, Kümmel S, Musat F, Richnow HH, Musat N. Calculation of Single Cell Assimilation Rates From SIP-NanoSIMS-Derived Isotope Ratios: A Comprehensive Approach. Front Microbiol [Internet]. 2018 [cited 2023 Mar 31];9. Available from: https://www.frontiersin.org/articles/10.3389/fmicb.2018.02342

42. Musat N, Stryhanyuk H, Bombach P, Adrian L, Audinot JN, Richnow HH. The effect of FISH and CARD-FISH on the isotopic composition of 13C- and 15N-labeled Pseudomonas putida cells measured by nanoSIMS. Syst Appl Microbiol. 2014 Jun 1;37(4):267–76.

43. Haouari O, Fardeau ML, Cayol JL, Fauque G, Casiot C, Elbaz-Poulichet F, et al. Thermodesulfovibrio hydrogeniphilus sp. nov., a new thermophilic sulphate-reducing bacterium isolated from a Tunisian hot spring. Syst Appl Microbiol. 2008 Mar 19;31(1):38–42.

44. Miller HM, Chaudhry N, Conrad ME, Bill M, Kopf SH, Templeton AS. Large carbon isotope variability during methanogenesis under alkaline conditions. Geochim Cosmochim Acta. 2018 Sep 15;237:18–31.

663 45. Lester Jr. W, Sun SH, Seber A. Observations on the Influence of Deuterium on Bacterial
664 Growth*. Ann N Y Acad Sci. 1960;84(16):667–77.

665 46. Pernice M, Dunn SR, Tonk L, Dove S, Domart-Coulon I, Hoppe P, et al. A nanoscale
666 secondary ion mass spectrometry study of dinoflagellate functional diversity in reef-building
667 corals. Environ Microbiol. 2015;17(10):3570–80.

668 47. Englander SW, Sosnick TR, Englander JJ, Mayne L. Mechanisms and uses of hydrogen
669 exchange. Curr Opin Struct Biol. 1996 Feb;6(1):18–23.

670 48. Bai Y, Milne JS, Mayne L, Englander SW. Primary structure effects on peptide group
671 hydrogen exchange. Proteins Struct Funct Bioinforma. 1993;17(1):75–86.

672 49. Cui D, Kong L, Wang Y, Zhu Y, Zhang C. In situ identification of environmental
673 microorganisms with Raman spectroscopy. Environ Sci Ecotechnology. 2022 Jul
674 1;11:100187.

675 50. Mosier-Boss PA. Review on SERS of Bacteria. Biosensors. 2017 Dec;7(4):51.

676 51. Wang K, Chen L, Ma X, Ma L, Chou KC, Cao Y, et al. Arcobacter Identification and Species
677 Determination Using Raman Spectroscopy Combined with Neural Networks. Appl Environ
678 Microbiol. 2020 Oct;86(20):e00924-20.

679 52. Novelli-Rousseau A, Espagnon I, Filiputti D, Gal O, Douet A, Mallard F, et al. Culture-free
680 Antibiotic-susceptibility Determination From Single-bacterium Raman Spectra. Sci Rep. 2018
681 Mar 2;8(1):3957.

682 53. Klein F, Humphris SE, Guo W, Schubotz F, Schwarzenbach EM, Orsi WD. Fluid mixing and
683 the deep biosphere of a fossil Lost City-type hydrothermal system at the Iberia Margin. Proc
684 Natl Acad Sci. 2015 Sep 29;112(39):12036–41.

685 54. Hatzenpichler R, Krukenberg V, Spietz RL, Jay ZJ. Next-generation physiology approaches
686 to study microbiome function at single cell level. Nat Rev Microbiol. 2020 Apr;18(4):241–56.

687 55. Cui L, Yang K, Zhou G, Huang WE, Zhu YG. Surface-Enhanced Raman Spectroscopy
688 Combined with Stable Isotope Probing to Monitor Nitrogen Assimilation at Both Bulk and
689 Single-Cell Level. Anal Chem. 2017 Jun 6;89(11):5793–800.

690 56. Ivleva NP, Kubryk P, Niessner R. Raman microspectroscopy, surface-enhanced Raman
691 scattering microspectroscopy, and stable-isotope Raman microspectroscopy for biofilm
692 characterization. Anal Bioanal Chem. 2017 Jul 1;409(18):4353–75.

693 57. Wang Y, Huang WE, Cui L, Wagner M. Single cell stable isotope probing in microbiology
694 using Raman microspectroscopy. Curr Opin Biotechnol. 2016 Oct 1;41:34–42.

695 58. Weber F, Zaliznyak T, Edgcomb VP, Taylor GT. Using Stable Isotope Probing and Raman
696 Microspectroscopy To Measure Growth Rates of Heterotrophic Bacteria. Appl Environ
697 Microbiol. 2021 Oct 28;87(22):e01460-21.

698 59. Wang Y, Xu J, Kong L, Liu T, Yi L, Wang H, et al. Raman–deuterium isotope probing to
699 study metabolic activities of single bacterial cells in human intestinal microbiota. Microb
700 Biotechnol. 2020;13(2):572–83.

701 60. Chisanga M, Muhamadali H, Ellis DI, Goodacre R. Surface-Enhanced Raman Scattering
702 (SERS) in Microbiology: Illumination and Enhancement of the Microbial World. Appl
703 Spectrosc. 2018 Jul 1;72(7):987–1000.

704 61. Chisanga M, Muhamadali H, Kimber R, Goodacre R. Quantitative detection of isotopically
705 enriched E. coli cells by SERS. Faraday Discuss. 2017 Nov 30;205(0):331–43.

706 62. Efrima S, Zeiri L. Understanding SERS of bacteria. J Raman Spectrosc. 2009;40(3):277–88.

707 63. Mosier-Boss PA, Sorensen KC, George RD, Obraztsova A. SERS substrates fabricated using
708 ceramic filters for the detection of bacteria. Spectrochim Acta A Mol Biomol Spectrosc. 2016
709 Jan 15;153:591–8.

710 64. Kubryk P, Kölschbach JS, Marozava S, Lueders T, Meckenstock RU, Niessner R, et al.
711 Exploring the Potential of Stable Isotope (Resonance) Raman Microspectroscopy and Surface-
712 Enhanced Raman Scattering for the Analysis of Microorganisms at Single Cell Level. Anal
713 Chem. 2015 Jul 7;87(13):6622–30.

714 65. Hu F, Shi L, Min W. Biological imaging of chemical bonds by stimulated Raman scattering
715 microscopy. Nat Methods. 2019 Sep;16(9):830–42.

716 66. Cicerone M. Molecular imaging with CARS micro-spectroscopy. Curr Opin Chem Biol. 2016
717 Aug 1;33:179–85.

718 67. Camp Jr CH, Cicerone MT. Chemically sensitive bioimaging with coherent Raman scattering.
719 Nat Photonics. 2015 May;9(5):295–305.

720 68. Ivleva NP, Wagner M, Horn H, Niessner R, Haisch C. Raman microscopy and surface-
721 enhanced Raman scattering (SERS) for in situ analysis of biofilms. J Biophotonics. 2010;3(8–
722 9):548–56.

723 69. Weiss R, Palatinszky M, Wagner M, Niessner R, Elsner M, Seidel M, et al. Surface-enhanced
724 Raman spectroscopy of microorganisms: limitations and applicability on the single-cell level.
725 Analyst. 2019;144(3):943–53.

726 70. Kilburn MR, Wacey D. CHAPTER 1 Nanoscale Secondary Ion Mass Spectrometry
727 (NanoSIMS) as an Analytical Tool in the Geosciences. 2014;1–34.

728